

Storm-Associated Microwave Radiometric Signatures in the Frequency Range of 90–220 GHz

J. R. WANG

Laboratory for Hydrospheric Processes, NASA/Goddard Space Flight Center, Greenbelt, Maryland

J. ZHAN

Caelum Research Corporation, Silver Spring, Maryland

P. RACETTE

Laboratory for Hydrospheric Processes, NASA/Goddard Space Flight Center, Greenbelt, Maryland

(Manuscript received 8 December 1995, in final form 20 June 1996)

ABSTRACT

Radiometric measurements were made by a millimeter-wave imaging radiometer (MIR) at the frequencies of 89, 150, 183.3 ± 1 , 183.3 ± 3 , 183.3 ± 7 , and 220 GHz aboard the NASA ER-2 aircraft at an altitude of about 20 km over two rainstorms: one in the western Pacific Ocean on 19 January 1993 and another in southern Florida on 5 October 1993. These measurements were complemented by nearly simultaneous observations by other sensors aboard the same aircraft and another aircraft flying along the same path. Analysis of data from these measurements, aided by radiative transfer and radar reflectivity calculations of hydrometeor profiles, which are generated by a general cloud ensemble model, demonstrates the utility of these frequencies for studying the structure of frozen hydrometeors associated with storms. Particular emphasis is placed on the three water vapor channels near 183.3 GHz. Results show that the radiometric signatures measured by these channels over the storm-associated scattering media bear a certain resemblance to those previously observed over a clear and fairly dry atmosphere with a cold ocean background. Both of these atmospheric conditions are characterized by a small amount of water vapor above a cold background. Radiative transfer calculations were made at these water vapor channels for a number of relative humidity profiles characterizing dry atmospheres over an ocean surface. The results are compared with the measurements to infer some characteristics of the environment near the scattering media. Furthermore, radiometric signatures from these channels display unique features for towering deep convective cells that could be used to identify the presence of such cells in storms.

1. Introduction

Microwave radiometric measurements of precipitation have been conducted from both aircraft and satellite platforms for nearly two decades (Wilheit et al. 1977, 1982; Rodgers et al. 1979; Prabhakara et al. 1986; Spencer 1986; Spencer et al. 1989; Adler et al. 1990; Weinman and Guetter 1977; Chang et al. 1993; Vivekanandan et al. 1993). Radiative transfer calculations based on simple hydrometeor profiles or more sophisticated profiles derived from general cloud ensemble models have been made to interpret the observed radiometric signatures (Wilheit et al. 1977, 1991; Smith and Mugnai 1988; Yeh et al. 1990). Furthermore, from the activities associated with the Tropical Rainfall Measuring Mission (TRMM) program (Simpson et al. 1988), a number of

algorithms have been developed to retrieve the rain rate from microwave radiometric measurements (Weinman et al. 1990; Wilheit et al. 1991; Smith et al. 1992; Kummerow et al. 1989; Kummerow and Giglio 1994). Most of these efforts emphasize using radiometric signatures at frequencies below 90 GHz. The signatures of rain are mainly caused by the emission of microwave radiation by liquid hydrometeors that gives rise to warm radiometric brightness over a cold ocean background (Wilheit et al. 1977). Moderate signatures caused by scattering processes at 37 and 85 GHz are also used to estimate rain rate over land surface (Spencer 1986; Spencer et al. 1989; Adler et al. 1993; Negri et al. 1994).

Radiometric signatures of precipitating systems at frequencies of 90 GHz or greater have not been explored as extensively; to the best of our knowledge, only a few studies have been reported in the literature. Wilheit et al. (1982), Hakkarinen and Adler (1988), and Adler et al. (1990) have examined radiometric signatures at both 90- and 183-GHz frequencies from, respectively, Trop-

Corresponding author address: Dr. James R. Wang, NASA/Goddard Space Flight Center, Code 975, Greenbelt, MD 20771.
E-mail: wang@sensor.gsfc.nasa.gov

ical Storm Cora and a deep convective storm on the east coast of the United States. Wang et al. (1994) also reported observations of these signatures from Super-typhoon Flo near Okinawa, Japan. Prasad et al. (1995) made radiative transfer calculations and compared the results with aircraft observations at these frequencies. Bauer and Grody (1995) combined the measurements of the Special Sensor Microwave/Imager (SSM/I) and the 91- and 183.3 ± 7 -GHz channels of the Special Sensor Microwave Temperature Sounder-2 (SSM/T2) aboard the Defense Meteorological Satellite Program (DMSP) *F-11* satellite to improve identification of snowcover and precipitation. All of these studies have contributed to our understanding of some unique features associated with scattering of radiation near 90 and 183 GHz by frozen hydrometeors. However, the rich information contained in these high-frequency observations over rainstorms remains to be explored fully. This is especially true as the recently developed Millimeter-wave Imaging Radiometer (MIR) provides not only much better temperature sensitivity but two additional channels of measurements at 150 and 220 GHz (Racette et al. 1996; Wang et al. 1995). A recent research effort by Heymsfield et al. (1996) used the MIR measurements at three window channels of 89, 150, and 220 GHz. They observed a correlation between the brightness temperatures at these frequencies and the average 9.7-GHz EDOP radar (NASA ER-2 Doppler radar) reflectivity at 6–10-km altitudes over rain cells, which was similar to the results reported by Wang et al. (1994). The utility of measurements from the 183.3-GHz water vapor channels has not been emphasized or explored by these authors.

In this paper, we report observations by a host of airborne microwave radiometers over two rainstorms, one over the western Pacific Ocean near the equator and another over southern Florida. Emphasis is placed on measurements made by the MIR. In particular, the potential of the water vapor channels to infer the properties of the frozen hydrometeors is examined in some detail. The advantage of utilizing data from these water vapor channels is illustrated by both radiative transfer calculations and measurements. The ER-2 aircraft flights over the region in southern Florida also include measurements from EDOP that provide radar reflectivity profiles in 2-s intervals. The relation between the measurements of EDOP and MIR water vapor channels is explored and discussed.

2. The measurements

Two cases of measurements were selected for this study; both cases cover a brief period of observations over a towering convective cell. The first case, on 19 January 1993, occurred during a period when NASA deployed two research aircraft, DC-8 and ER-2, in the western Pacific to make supporting measurements of atmospheric and oceanic parameters during the intensive

observation period of the Tropical Ocean Global Atmosphere Coupled Ocean–Atmosphere Response Experiment (TOGA COARE). Both aircraft were stationed in Townsville, Australia. In addition to other instrumentation, there were several microwave radiometers aboard these aircraft. On the DC-8 aircraft, there were two radiometer systems: Airborne Multichannel Microwave Radiometer (AMMR), an assembly of single-beam radiometers at the frequencies of 10, 18.7, 22, 37, and 92 GHz; and Airborne Microwave Moisture Sounder (AMMS), a four-channel cross-track imager at the frequencies of 92, 183.3 ± 2 , 183.3 ± 5 , and 183.3 ± 9 GHz. A description of the operation and calibration of AMMR and AMMS can be found in Wang et al. (1994) and references therein. The temperature sensitivity for each channel of AMMR, for an integration period of 1 s, is better than 1 K with calibration accuracy of about ± 3 K. The sensitivity of the AMMS at an integration period of 70 ms is about 4–5 K, with calibration accuracy on the order of ± 2 K. These two instruments have been flown either independently or together in various configurations and aircraft platforms for more than a decade (Wilheit et al. 1982; Wang et al. 1983, 1994; Kakar 1983; Lutz et al. 1991; Chang et al. 1993). Aboard the ER-2 aircraft were two imaging radiometers: MIR, a total power radiometer that scans across track with an angular swath of 100° centered at nadir (Racette et al. 1996), and Advanced Microwave Precipitation Radiometer (AMPR), a cross-track scanner that measures radiation at the frequencies of 10.7, 19.35, 37.1, and 85 GHz. A detailed description of the AMPR system can be found in Spencer et al. (1994). MIR has six frequency channels at 89, 150, 183.3 ± 1 , 183.3 ± 3 , 183.3 ± 7 , and 220 GHz. It has a temperature sensitivity of less than or equal to 1 K based on a 70-ms integration time and a measurement accuracy of ± 2 K or better. The MODIS (Moderate Resolution Imaging Spectrometer) Airborne Simulator (MAS) was also aboard the ER-2 aircraft; the data acquired by a thermal infrared channel ($13 \mu\text{m}$) of this instrument were included in the following analysis. The ER-2 aircraft was flying at a nominal altitude of 20 km, while the flight altitude of the DC-8 aircraft varied between 3 and 12 km according to specific requirements.

The flight on 19 January 1993 over a rainstorm in the equatorial region of the western Pacific was coordinated so that the ER-2 aircraft was flying almost directly above the DC-8 aircraft along the same path. The speeds of the DC-8 and ER-2 aircraft are about 264 and 217 m s^{-1} , respectively. The flight segment from west by northwest to east by southeast, as shown in Fig. 1, indicates that the passage of the two aircraft over the same locations differs by no more than 3–4 min. The coincident flight paths allow a direct comparison of radiometric signatures at comparable frequencies. The figure also shows the distribution of the 5.996-GHz radar reflectivity in gray scale at the height of 1 km obtained by the NOAA P3 aircraft over the region during the

P3 - LF COMPOSITE JAN 19, 1993 0448 UTC TO 0502 UTC

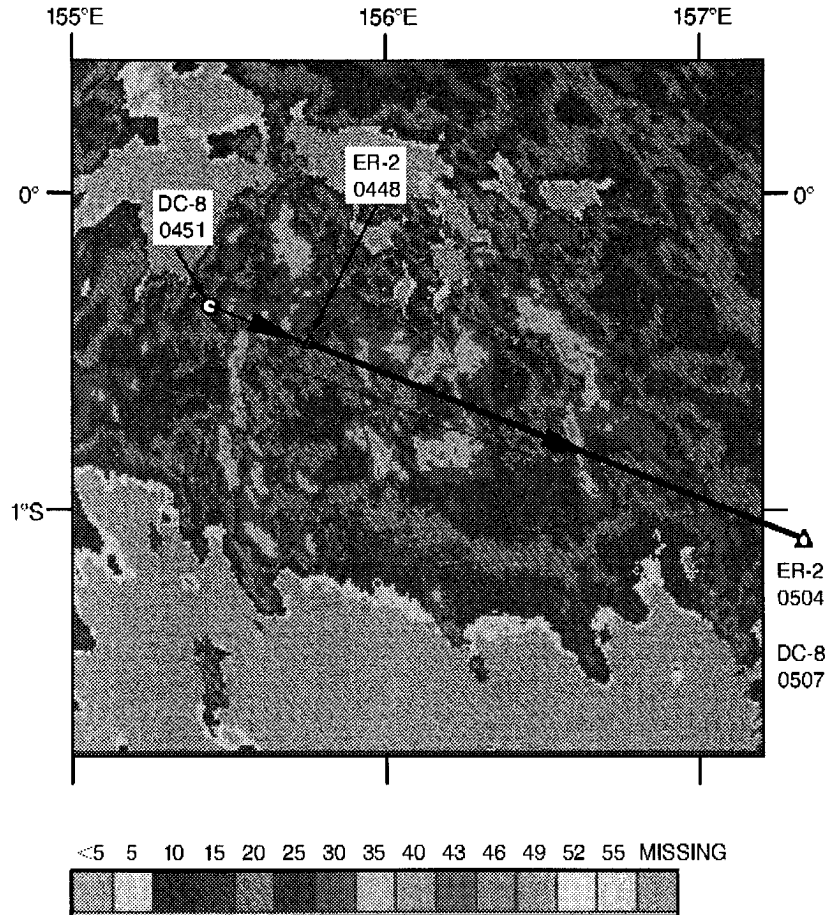


FIG. 1. The flight paths of the NASA ER-2 and DC-8 aircraft on 19 January 1993 overlaying the LF composite reflectivity map generated by the NOAA P3 radar.

period of 0448–0502 UTC, in near concurrence with the ER-2 and DC-8 aircraft flights. A few cells of strong radar reflectivity were directly overflowed by both NASA aircraft. A dropsonde was released from the DC-8 aircraft around 0450 UTC at the location 0.32°S , 155.29°E . Rawinsonde observations at several locations near the area of the aircraft flights were made around 0600 UTC.

The temperature and relative humidity profiles obtained from both dropsonde and rawinsondes are plotted in Fig. 2a and 2b, respectively. The profiles derived from the rawinsondes are denoted by the dashed curves. They are the averages of the profiles from two stations, R/V *Kexue* (ship) at 3.95°S , 155.99°E , and Kapingamarangi (island) at 1.07°S , 154.80°E ; these are stations installed specifically for TOGA COARE. The profiles derived from the dropsonde are given by the dash-dotted curves; the temperature profile from dropsonde at altitudes be-

low 10 km is nearly identical to the one derived from the rawinsonde observations and is, therefore, not shown. The solid curves give the averages of the 78 pairs of temperature and humidity profiles generated by tropical cloud model, which are used as input parameters for radiative transfer calculations in the next section. Over the altitude range of 0–18 km, the average model-derived temperature profile is about 2–5 K higher than that from observations. The relative humidity profile from the dropsonde is quite comparable to the one generated by the tropical cloud model and assumes a nearly constant value of 85% from surface to 10-km altitude. On the other hand, the average relative humidity profile provided by the nearby rawinsonde stations gives a much drier air at altitudes above 5 km.

In the second study case, only the NASA ER-2 aircraft was involved and the measurements were made on

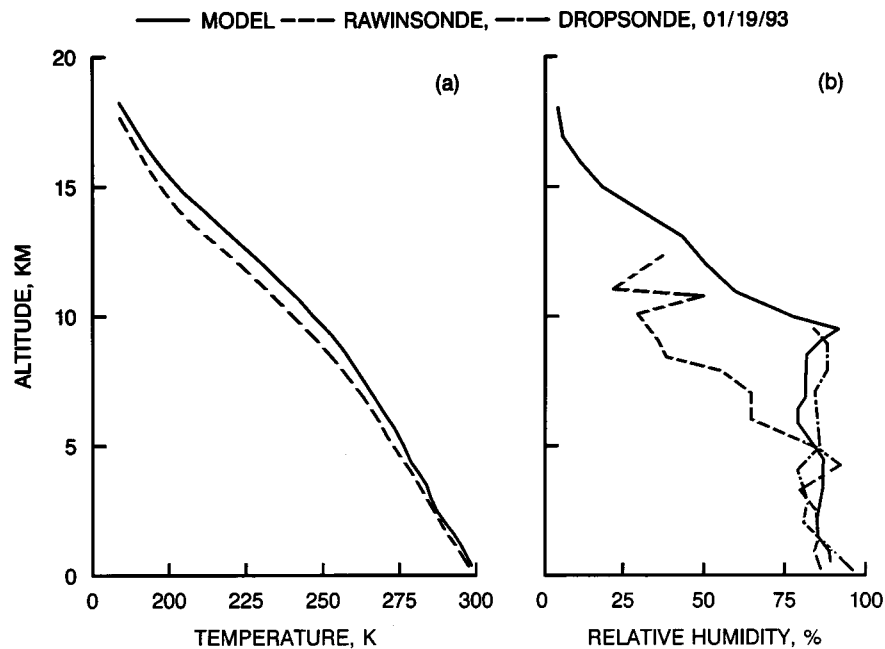


FIG. 2. The temperature and relative humidity profiles observed by rawinsondes and dropsonde near the region of aircraft flights on 19 January 1993. The solid curves are the average profiles generated from the RAMS model.

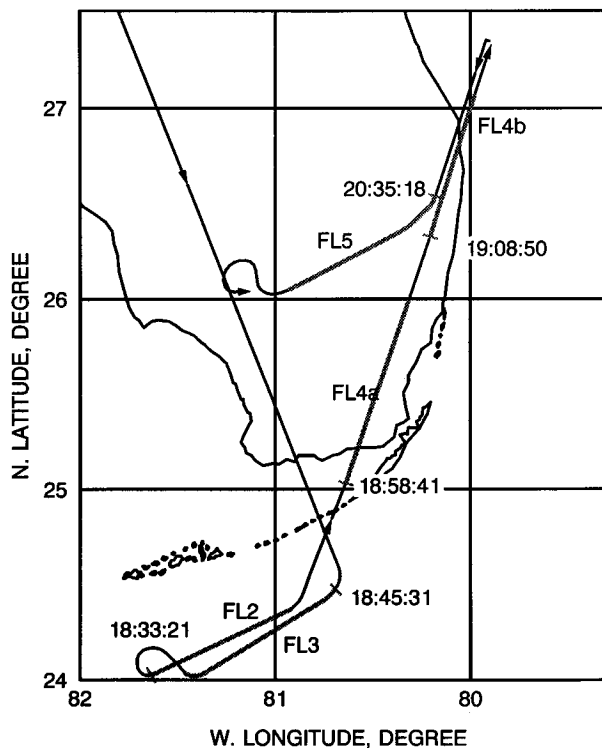


FIG. 3. A sketch showing the ER-2 flight path over southern Florida. The tick marks give the beginning times of the five flight segments over regions of precipitation.

5 October 1993 over both land and ocean surfaces in southern Florida. The ER-2 aircraft was stationed at the NASA Wallops Flight Facility in Wallops Island, Virginia, for the Convection and Atmospheric Moisture Experiment (CAMEX). Aboard the aircraft were a number of instrument packages relevant to the present study including the MIR, the EDOP, and the Multispectral Atmospheric Mapping Sensor (MAMS). Figure 3 shows the portion of the ER-2 aircraft flight path that includes five segments, designated by FL2, FL3, FL4a, FL4b, and FL5, over regions of precipitation. The times in the figure refer to the tick marks at the beginning of the flight segments. The EDOP was operational only in the first four segments; it was turned off after the completion of the flight segment FL4b because of interference with AMPR aboard the same aircraft. Both MIR and MAMS functioned normally throughout the entire flight.

The rawinsonde launches at West Palm Beach and Key West were made only at the regular times around 0000 and 1200 UTC, not close to the time of the aircraft flight. The one acquired at 0000 UTC 6 October 1993 had missing data at high altitudes. Therefore, the more complete temperature and relative humidity profiles from the 1200 UTC observations on 5 October are shown in Fig. 4. The temperature profiles from the two stations represented by the solid curve are very close. These temperature profiles are quite different from those measured in the western Pacific shown in Fig. 2; at altitudes below 12 km, the profiles from the western Pacific give a higher temperature than those from southern Florida, while at altitudes above 12 km the trend

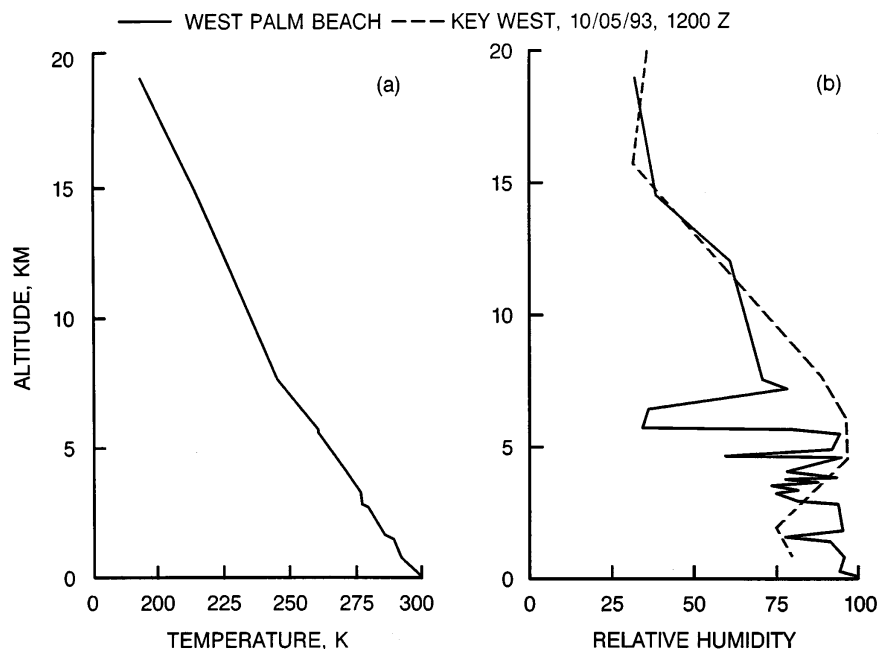


FIG. 4. The temperature and relative humidity profiles at West Palm Beach and Key West acquired by rawinsondes at 1200 UTC 5 October 1993. The temperature profiles from both Key West and West Palm Beach are almost identical.

reverses. The relative humidity profiles in plot (b) of Fig. 4 show values greater than or equal to 30% at the altitude range of 15–20 km. There are no data in the same altitude range from the rawinsondes shown in Fig. 2. If the relative humidity in that altitude range is not significantly greater than 30% in the western Pacific, then the upper atmosphere over southern Florida would hold more water vapor because of the higher temperatures. This appears to be the situation implied by the observations of the MIR water vapor channels described and discussed in the following sections.

3. Model simulation

To help gain a basic understanding of the radiometric signatures at the MIR water vapor channels as well as the radar reflectivities of EDOP, three-dimensional tropical convective cell simulations were performed using the University of Wisconsin version of the Regional Atmospheric Modeling System (RAMS) (Tripoli 1992). RAMS is a three-dimensional, time-dependent nonhydrostatic mesoscale cloud model incorporating explicit microphysical processes. It is initialized with input of the temperature and relative humidity profiles derived from a tropical climatology model (McClatchey et al. 1972). The microphysical component of the RAMS model is the comprehensive phase bulk parameterization described by Cotton et al. (1986). The RAMS model generates ice liquid water, potential temperature, and mixing ratios of water, rain, ice, snow, graupel, and hail. Cloud water, water vapor, dry-air density, potential tem-

perature, and temperature are determined diagnostically on the assumption of zero supersaturation with respect to water and to the instantaneous growth and evaporation of cloud drops in response to changes in supersaturation (Tripoli 1992; Smith et al. 1992). A microphysical output from the model provides in detail the liquid and ice water content information for cloud, rain, ice, snow, graupel, and hail from surface to 18.5-km altitude. A total of 78 simulated outputs of hydrometeor, temperature, and relative humidity profiles (E. A. Smith and X. Xiang 1994, personal communication) are generated for this study. The average values of these temperature and relative humidity profiles are entered in Fig. 2 for comparison with those from rawinsonde and dropsonde observations.

A RAMS model-produced cross section of cloud, rain, ice, snow, graupel, and hail is shown in Fig. 5. This particular set is the most intense among the 78 sets produced by the RAMS cloud model. The hail is not present in this set. The most prominent feature is that the graupels are updrafted and rimed together in the altitude range of 4–14 km with a maximum ice water content of 0.7 g m^{-3} in the altitude range of 6–9 km. The snow particles are distributed in the same altitude range with a maximum ice water content of 0.15 g m^{-3} . The rain profile in the 1.5–5.5-km altitude range is quite moderate, peaking at about 4-km height with a water content of 0.17 g m^{-3} . The concentration of hydrometeors in this and the remaining 77 sets of RAMS model-produced outputs is mostly limited to altitudes below 12 km. These features of cloud microphysics have been

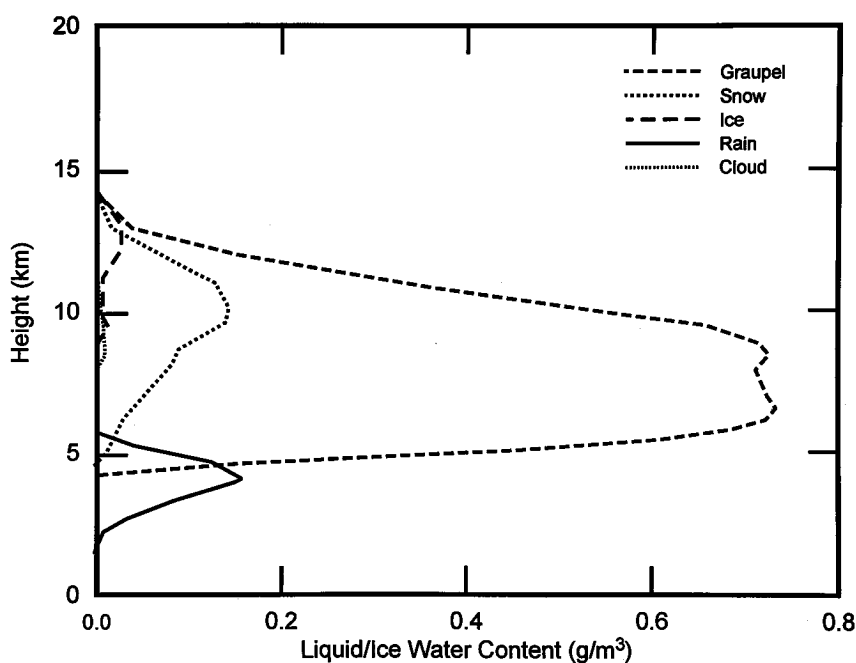


FIG. 5. One of the 78 profiles of hydrometeors produced by the RAMS cloud model (Tripoli 1992).

implied by several authors (Adler et al. 1990; Vivekanandan et al. 1993).

The upwelling brightness temperature $T_b(\nu)$ at the frequency ν at the top of the atmosphere was calculated for the MIR window channels at 89, 150, and 220 GHz, using a radiative transfer that incorporated Eddington's second approximation (Wu and Weinman 1984; Kummerow 1993). It was found that the calculated $T_b(\nu)$ values did not show as strong frequency dependence as those observed by the MIR. To arrive at the calculated $T_b(\nu)$ values comparable to those observed at all six MIR frequencies would require a modification of parameters, such as the size distribution of hydrometeors, in the RAMS cloud model, which is beyond the scope of the present analysis. The calculated $T_b(\nu)$'s at the three water vapor channels, on the other hand, are quite comparable to the observed values. Therefore, the calculated results and the implications derived from the comparison with observations to be described in the following are limited to the water vapor channels. In addition, a procedure described by Olson et al. (1995) is also employed in the calculations of the radar reflectivities at the EDOP frequency of 9.7 GHz, using the same 78 sets of hydrometeor profiles generated by the RAMS cloud model. The results of these calculations for both $T_b(\nu)$'s in the water vapor channels and reflectivity profiles are summarized in Figs. 6 and 7 and discussed below.

For convenience of discussion, the differences in $T_b(\nu)$ values between two frequency channels ν_1 and ν_2 are defined as

$$\Delta T_b(\nu_1, \nu_2) = T_b(\nu_1) - T_b(\nu_2). \quad (1)$$

Figure 6 shows the scatterplots of the calculated values between $\Delta T_b(183.3 \pm 1, 183.3 \pm 3)$ and $T_b(183.3 \pm 3)$, and between $\Delta T_b(183.3 \pm 3, 183.3 \pm 7)$ and $T_b(183.3 \pm 7)$; plots (a) and (c) are for the former and plots (b) and (d) for the latter. To conform with the measurements, the effect of double side bands in the water vapor channels is taken into account by averaging the calculated values at $T_b(180.3)$ and $T_b(186.3)$ for $T_b(183.3 \pm 3)$. The data points represented by asterisks in plots (a) and (b) are values calculated by the original hydrometeor profiles generated from the RAMS cloud model, while those denoted by open circles are calculated values based on the same hydrometeor profiles of cloud, rain, ice, snow, graupel, and hail, but with relative humidity set equal to zero at all altitudes. Plots (c) and (d) give the results of calculations based on modified hydrometeor profiles in which the relative humidity profiles remain the same, while the profiles of graupel, ice, snow, cloud, and hail are extended to a higher altitude by 3 km. This modification of hydrometeor profiles is needed to compare the calculated $T_b(\nu)$ values in the water vapor channels with those observed over the deep convective cells.

The calculated results in plots (a) and (b) of Fig. 6 clearly suggests that, to the first order, the responses of all three water vapor channels to cloud, rain, ice, snow, graupel, and hail are the same and that the increase in $\Delta T_b(183.3 \pm 1, 183.3 \pm 3)$ or $\Delta T_b(183.3 \pm 3, 183.3 \pm 7)$ with the decrease in $T_b(183.3 \pm 3)$ or $T_b(183.3 \pm 7)$ is caused by water vapor absorption. Plots (c) and (d) of the same figure show that as the frozen hydrometeor

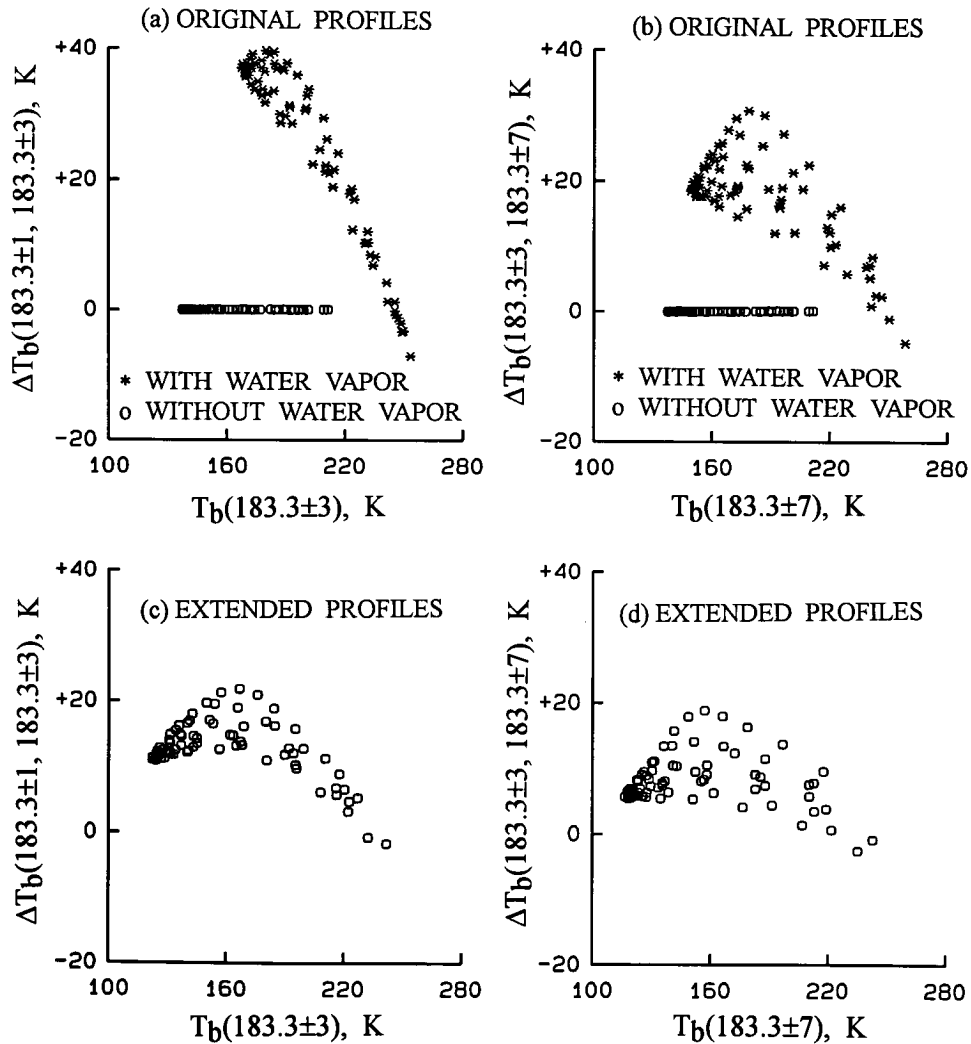


FIG. 6. The scatterplots of brightness temperature difference against brightness temperature for different pairs of water vapor channels. Plots (a) and (b) are results calculated from the original model-generated hydrometeor profiles, while plots (c) and (d) are calculated results with the frozen hydrometeor profiles extended upward by 3 km.

profiles are extended to higher altitudes, the $\Delta T_b(183.3 \pm 1, 183.3 \pm 3)$ and $\Delta T_b(183.3 \pm 3, 183.3 \pm 7)$ values either level off or decrease with further decrease in $T_b(183.3 \pm 3)$ and $T_b(183.3 \pm 7)$. This is due to the fact that the amount of water vapor above the hydrometeors is smaller in the modified profiles simulating the strong convective updraft.

Figure 7 shows the variations of $\Delta T_b(183.3 \pm 1, 183.3 \pm 3)$ and $\Delta T_b(183.3 \pm 3, 183.3 \pm 7)$ with the calculated average reflectivity at the EDOP frequency and integrated average ice water content (IWC) over the altitude range of 6–12 km. Only the results calculated from the original hydrometeor profiles are presented in this figure. It is clear from the figure that a significant correlation exists between $\Delta T_b(183.3 \pm 1, 183.3 \pm 3)$ or $\Delta T_b(183.3 \pm 3, 183.3 \pm 7)$ and the average EDOP reflectivity. On the other hand, a correlation between $\Delta T_b(183.3 \pm 1, 183.3$

$\pm 3)$ or $\Delta T_b(183.3 \pm 3, 183.3 \pm 7)$ and IWC is found only for $0 < \text{IWC} \leq 2.5 \text{ kg m}^{-2}$. At $\text{IWC} > 2.5 \text{ kg m}^{-2}$, $\Delta T_b(183.3 \pm 1, 183.3 \pm 3)$ and $\Delta T_b(183.3 \pm 3, 183.3 \pm 7)$ reach saturation values of approximately 40 and 25 K, respectively.

4. Results

a. The case of 19 January 1993

The data acquired from the six channels of the MIR along the ER-2 aircraft flight path indicated in Fig. 1 are displayed as six images in gray scale in Fig. 8. The vertical axis gives the elapsed time in minutes with respect to 0448 UTC, and the 14 min of data displayed here covers approximately a distance of 180 km. The width of each image corresponds to the MIR swath of

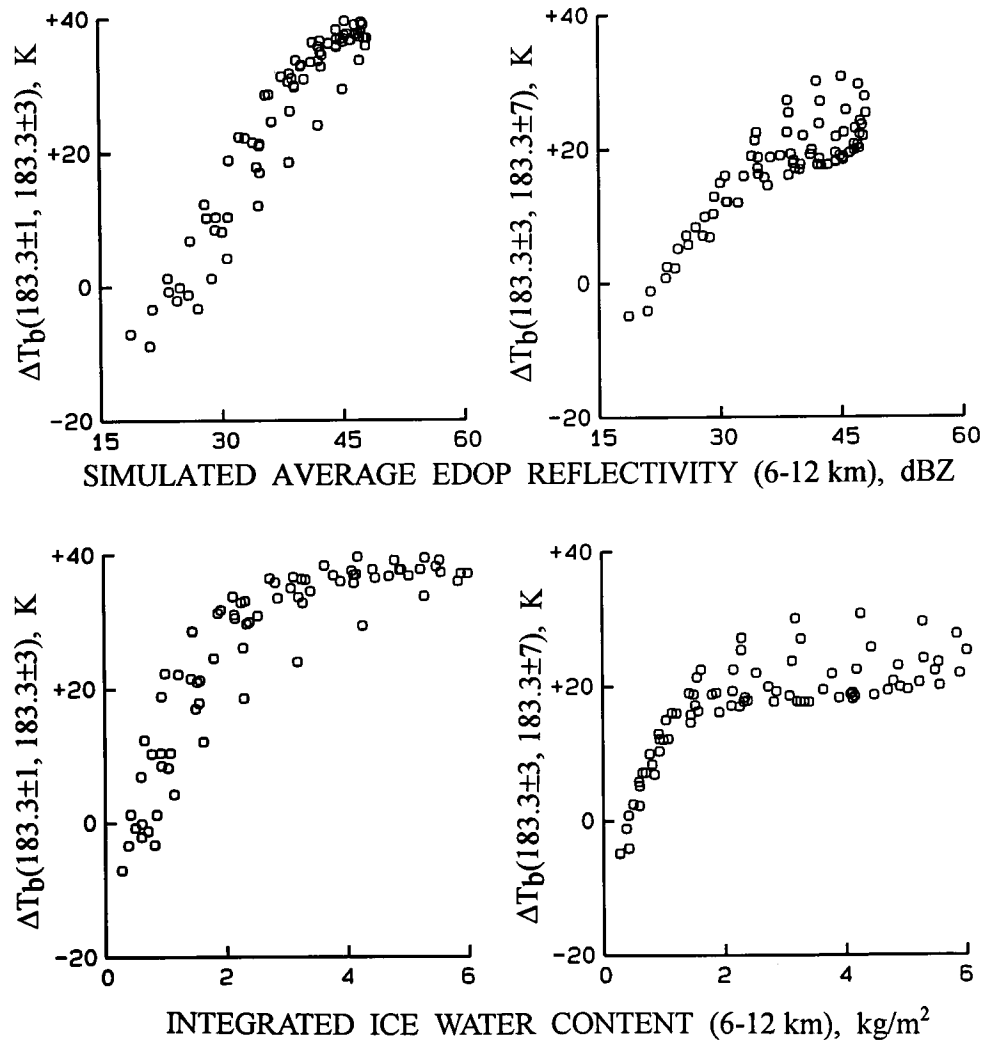


FIG. 7. The scatterplots showing the dependence of brightness temperature difference in the water vapor channels on average EDOP reflectivity and integrated ice water between the 6- and 12-km altitudes. All data are model simulated.

about 45 km at the surface of the earth. The frequency channels of the images are indicated in the bottom of the figure. To give a better temperature resolution in the display, the full gray scale is assigned to cover the $T_b(\nu)$ range of only 80 K, with wraparound occurring at the $T_b(\nu)$ values of 200 and 120 K. The contours of the wraparound are characterized by gradual darkening [decreasing $T_b(\nu)$] on one side and a sudden change to light color at even lower $T_b(\nu)$ values on the other side. For example, the high $T_b(183.3 \pm 1)$ values are about 240 K in the region between the elapsed times from 2 to 6 min; the lowest $T_b(183.3 \pm 1)$'s occur inside the 200-K wraparound contour right after the 6-min elapsed time. At 89 GHz, the highest values are approximately 280 K around 10-min elapsed time, and the lowest ones are inside the 200 wraparound contour around 6-min elapsed time. From these images one can identify three major regions of scattering signatures characterized by

low $T_b(\nu)$ values at the elapsed time intervals of 0–1, 6–8, and 11–14 min. The middle one of the three regions has the strongest scattering signatures with some $T_b(220)$ values less than 120 K right after the 6-min elapsed time.

Figure 9 shows the variations of $T_b(\nu)$ values at nadir measured by the MIR and MAS aboard the ER-2 aircraft (20-km altitude) between the period of 0446:34 and 0457:02 UTC: the top section for the 13- μm channel of the MAS and the 220 GHz of MIR; the middle section for the 89, 150, and 183.3 \pm 3 GHz of the MIR; and bottom section for the $\Delta T_b(\nu_1, \nu_2)$'s between the channels near 183.3 GHz. There is a strong correlation among all the MIR channels as expected, especially in the regions of scattering characterized by low $T_b(\nu)$ values. The $\Delta T_b(\nu_1, \nu_2)$'s in the bottom of the figure generally show an inverse relationship with the $T_b(\nu)$'s; that is, the lower the $T_b(\nu)$ values the larger the $\Delta T_b(\nu_1, \nu_2)$'s.

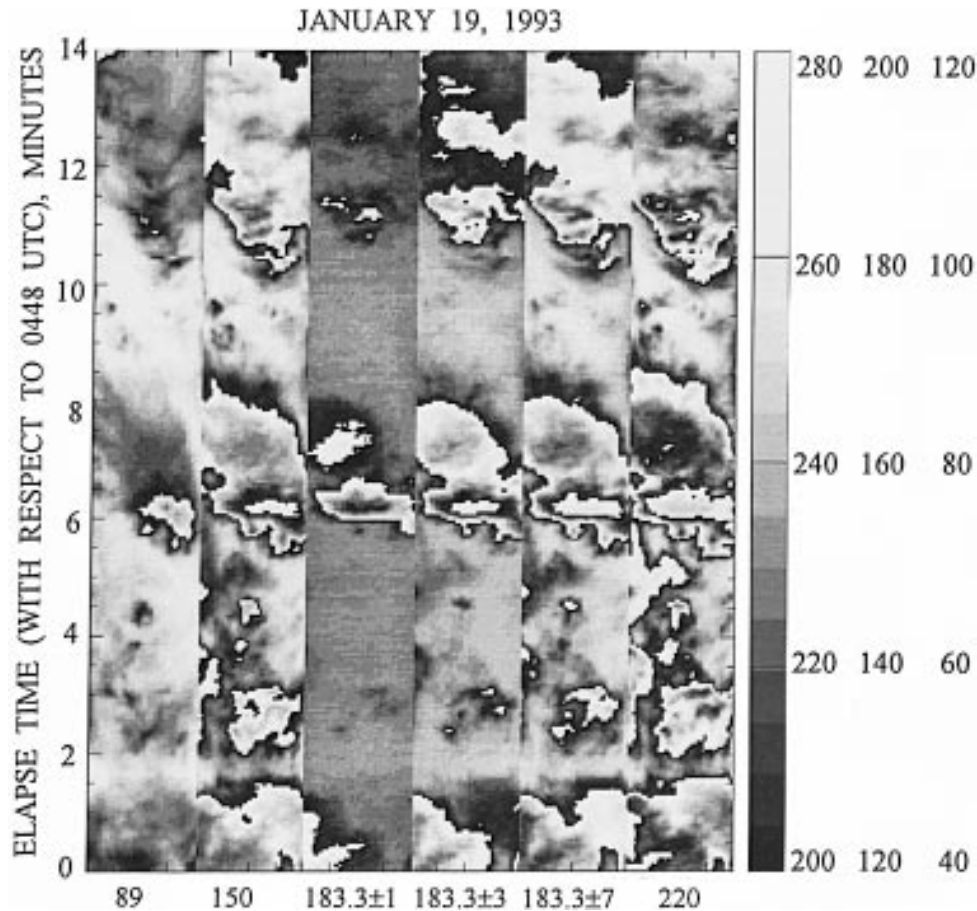


FIG. 8. Images showing the brightness temperature distribution at six MIR frequencies along the flight path indicated in Fig. 1. The elapse time along the vertical refers to 0448 UTC and the gray scale is wrapped around at the brightness temperature intervals of 80 K. The images cover a distance of about 180 km.

The most conspicuous departure from this trend occurs near 0454 UTC (as indicated by the vertical dashed line) where the lowest $T_b(\nu)$ values in all channels are observed and associated with the minima in $\Delta T_b(\nu_1, \nu_2)$'s. The measurements from the 13- μm channel of the MAS give values less than or equal to 190 K in that neighborhood. An examination of the P3 radar composite map at 15-km altitude also shows significant reflectivities near the location of the ER-2 aircraft at 0454 UTC. These observations imply the passage of the ER-2 aircraft over a towering convective cell with a significant updraft of hydrometeors that cause strong scattering of radiation at the MIR frequencies. Another distinct feature in the figure is the observation, throughout the entire period, of the small change in the 13- μm brightness and the large variation in $T_b(\nu)$'s at the MIR frequencies. The 13- μm brightness of about 210 K suggests a cloud top at approximately 14-km altitude, with the exception of the deep convective cell, based on the temperature profile in Fig. 2. These observations suggest that MIR frequencies are capable of providing a gross description

on the distribution of frozen hydrometeors below the cloud top.

Figure 10 shows the results of observations by the microwave radiometers aboard the DC-8 aircraft at 11-km altitude over the same region covered by the MIR as shown in Fig. 9. The variations of $T_b(\nu)$'s from the 91- and 183.3 \pm 5-GHz channels and the $\Delta T_b(\nu_1, \nu_2)$'s from the water vapor channels of the AMMS are displayed, respectively, at the top and bottom of the figure. The $T_b(\nu)$'s measured by the AMMR at 18, 21, and 37 GHz are shown in the middle part of the figure. It can be seen that the variations of the AMMS $T_b(\nu)$ values generally track well with those from the MIR in Fig. 9. At 90 GHz (for simplicity, a slight difference between 89 and 91 GHz of the two sensors is ignored), the $T_b(\nu)$'s from AMMS are generally higher than those from MIR over the cells of scattering [identified by the valleys of low $T_b(\nu)$]. The $T_b(\nu)$'s from the MIR could be smaller than those of AMMS by about 20–30 K at the centers of some scattering cells, implying the presence of a significant number of frozen hydrometeors in the layer

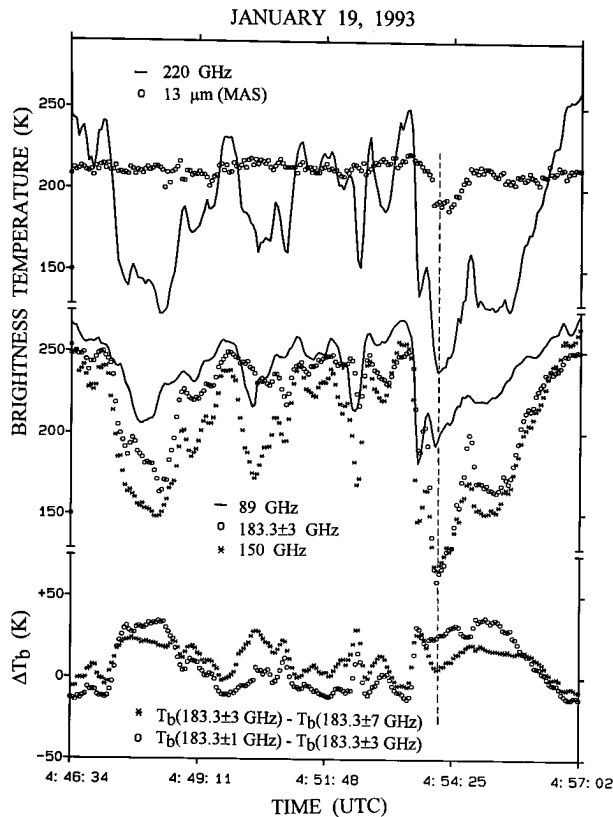


FIG. 9. Time variations of brightness temperatures observed by MIR and MAS aboard the ER-2 aircraft. The brightness temperature differences from the MIR water vapor channels are also included (1 min \approx 13 km).

between 11- and 20-km altitudes. The signatures at the three AMMR frequencies of 18, 21, and 37 GHz are more dominated by the liquid hydrometeors below the freezing level (Wilheit et al. 1982; Spencer et al. 1989). The presence of liquid hydrometeors, or rain, is associated with high $T_b(v)$ values at these frequencies, and it is clear from the figure that the occurrence of rain does not necessarily coincide with the concentration of frozen hydrometeors above the freezing level, which are associated with the strong depression in $T_b(v)$'s at the 183.3-GHz channels. Like the MIR data in Fig. 8, the $\Delta T_b(v_1, v_2)$'s from these channels again display an inverse relationship with the $T_b(v)$ values.

Figure 11 shows more explicitly the correlation between the $\Delta T_b(v_1, v_2)$'s and $T_b(v_2)$'s observed by the MIR at about the 20-km altitude. The plots (a) and (b) are, respectively, for $\Delta T_b(183.3 \pm 1, 183.3 \pm 3)$ and $T_b(183.3 \pm 3 \text{ GHz})$, and for $\Delta T_b(183.3 \pm 3, 183.3 \pm 7)$ and $T_b(183.3 \pm 7)$. Plot (c) is for $\Delta T_b(183.3 \pm 7, 220)$ and $T_b(220)$, and plot (d) is for $\Delta T_b(89, 150)$ and $T_b(150)$. Under clear-sky and moderately cloudy conditions, the lowest $T_b(v)$ values generally occur at $183.3 \pm 1 \text{ GHz}$ due to the absorption of atmospheric water vapor (Schaerer and Wilheit 1979; Wang et al. 1983), the $T_b(183.3 \pm 3)$'s are higher, and the $T_b(183.3 \pm 7)$'s

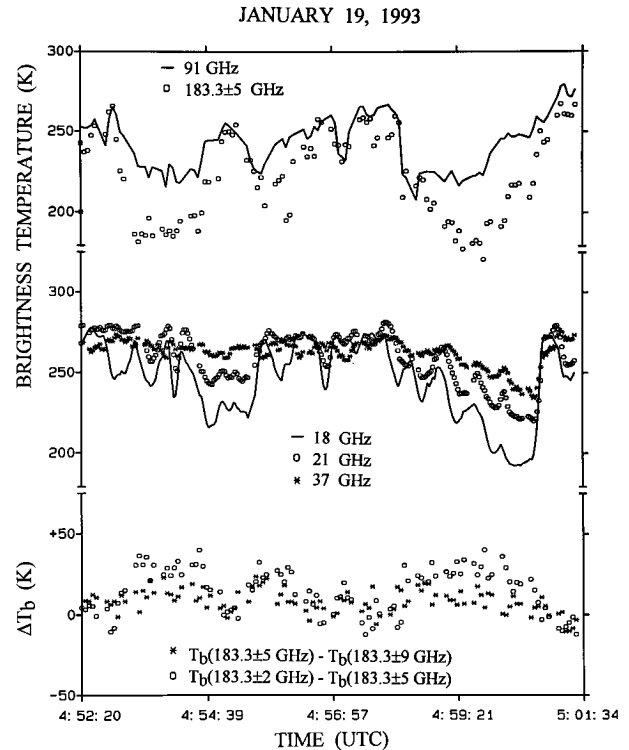


FIG. 10. Time variations of brightness temperatures observed by AMMS and AMMR aboard the DC-8 aircraft along the flight path shown in Fig. 1. The brightness temperature differences from the water vapor channels are also included in the figure (1 min \approx 16 km).

the highest among the three. These conditions correspond to the regions in plots (a) and (b) where the $\Delta T_b(183.3 \pm 1, 183.3 \pm 3)$ and $\Delta T_b(183.3 \pm 3, 183.3 \pm 7)$ are negative. Over the areas of precipitation with frozen hydrometeors that strongly scatter radiation and give rise to depression in $T_b(v)$ values at millimeter wavelengths, these differences become positive. This is due to the fact that the 183.3 ± 7 -GHz channel would view deeper into the layer of scattering than the 183.3 ± 1 -GHz channel. However, in both plots, the differences in $T_b(v)$'s become smaller with a further depression in the $T_b(v)$ values. In particular, toward the lowest $T_b(183.3 \pm 3)$ and $T_b(183.3 \pm 7)$ values of approximately 110 and 105 K, the $\Delta T_b(183.3 \pm 1, 183.3 \pm 3)$ and $\Delta T_b(183.3 \pm 3, 183.3 \pm 7)$ are only approximately 22 and 4 K, respectively. This suggests a significant reduction in the water vapor concentration above the scattering cell. Since it is very unlikely that the atmosphere would have a water vapor hole of a few kilometers in size, the scattering cell must be one with a strong updraft of hydrometeors to the 15–16-km region of diluted water vapor. This unique feature in the signatures of the 183.3-GHz channels is consistent with the observations of P3 radar and the 13- μm channel of the MAS around 0454 UTC (Fig. 9).

The relationship between $\Delta T_b(183.3 \pm 7, 220)$ and

MIR JANUARY 19, 1993 0444 - 0507 UTC
 o 04:53:20 - 04:56:15 UTC

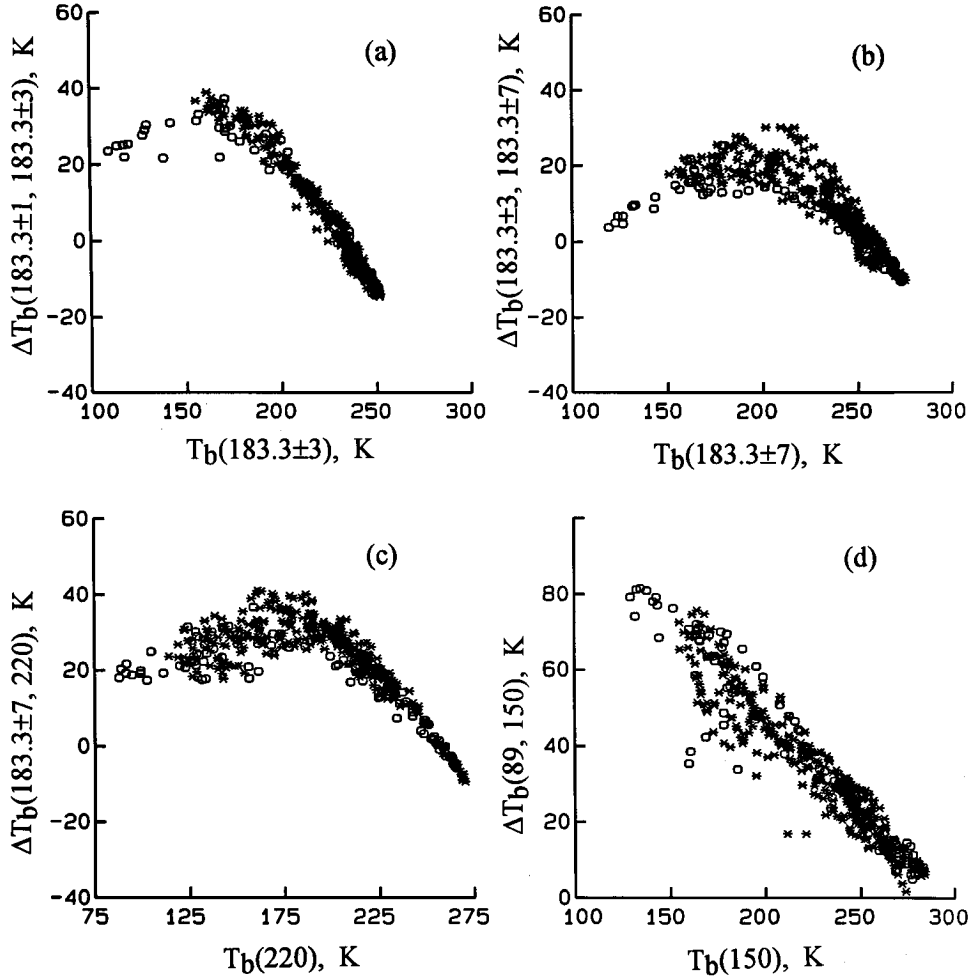


FIG. 11. The scatterplot of brightness temperature difference and brightness temperature from pairs of MIR channels.

$T_b(220)$ at the brightness range of 200–300 K displayed in plot (c) of Fig. 11 follows the same general pattern as that in plot (a) or (b) for a normal scattering cell. This is expected because the 220-GHz channel belongs to the far wing of the 183.3-GHz absorption feature. Over the convective cell with a strong updraft, the $\Delta T_b(183.3 \pm 7, 220)$ values converge not to zero, but to the value of about 18–20 K at the lowest $T_b(220)$ of about 110 K. Since the amount of water vapor above the scattering cell is small, this finite $\Delta T_b(183.3 \pm 7, 220)$ value is a direct consequence of the stronger scattering at 220 GHz than at 183.3 GHz. As we move away from the cell top, more and more water vapor comes in the path between the MIR and the scattering media. Here $T_b(183.3 \pm 7)$ increases faster than $T_b(220)$, and $\Delta T_b(183.3 \pm 7, 220)$ increases with the increase in

$T_b(220)$ until a broad maximum in $\Delta T_b(183.3 \pm 7, 220)$ is reached at the $T_b(220)$ value of about 200 K. The explanation of the observed feature in plot (d) is straightforward. In the region dominated by scattering with $T_b(150)$ of about 120 K, $\Delta T_b(89, 150)$ of about 80 K again is mainly caused by stronger scattering of radiation by hydrometeors at higher frequencies. As we move away from the cell top, water vapor in the region between MIR and the scattering cell increases. Here $T_b(150)$ increases more rapidly than $T_b(89)$ due to the stronger absorption at 150 than at 89 GHz, thus $\Delta T_b(89, 150)$ decreases with $T_b(150)$.

b. The case of the 5 October 1993

Heymsfield et al. (1996) have reported the measurements by EDOP, MAMS, AMPR (Spencer et al. 1994),

OCTOBER 5, 1993

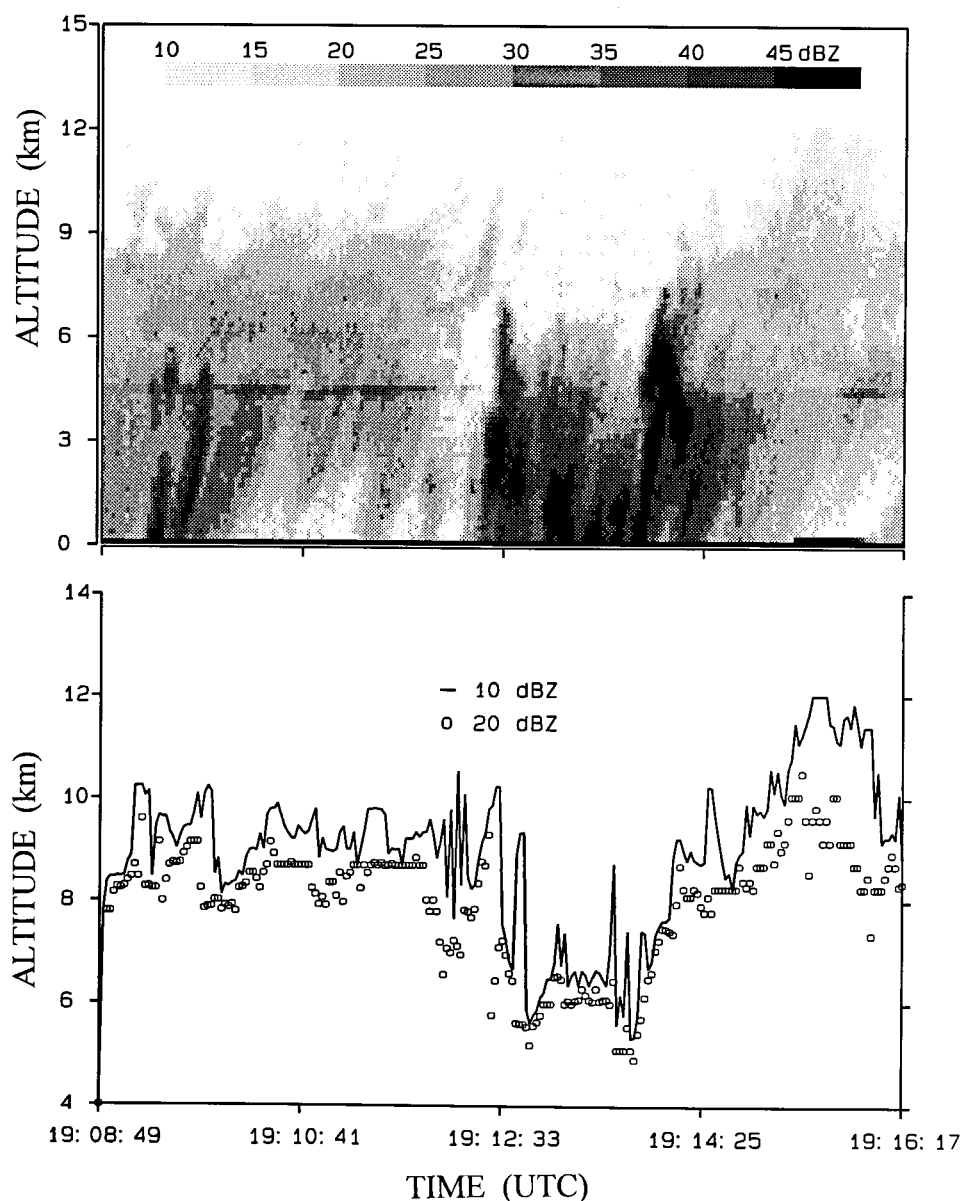


FIG. 12. EDOP reflectivity profiles and contours of constant reflectivity along the flight segment FL4b in Fig. 3 (1 min \approx 12 km).

and MIR over this particular rainstorm in Florida on 5 October 1993. Their analysis emphasized the response of EDOP and AMPR to rain, although a correlation, similar to that reported by Wang et al. (1994), was also found between $T_{b(v)}$'s measured at the 89- and 220-GHz channels of the MIR and the average EDOP reflectivity at 6–10-km altitudes. The signatures recorded by the three water vapor channels at 183.3 ± 1 , 183.3 ± 3 , and 183.3 ± 7 GHz of the MIR were not analyzed and reported by these authors. The radiometric signatures measured at these water vapor channels are found to correlate with reflectivities measured by the EDOP. This

correlation is significant in studying the properties of hydrometeors above the freezing level of the storm.

Figure 12 shows the profiles of the radar reflectivity Z observed by the EDOP along the flight segment FL4b indicated in Fig. 3. The top panel displays the spatial variation of the reflectivity profiles in gray scale along the flight path. The bottom panel gives, as viewed from the aircraft altitude, the variations of the reflectivity contours at 10 and 20 dBZ. The freezing level at the 4.5-km height is well defined by the bright band of the stratiform region (top panel of Fig. 12). As so often happened in typical rain storms, the freezing level is not well defined

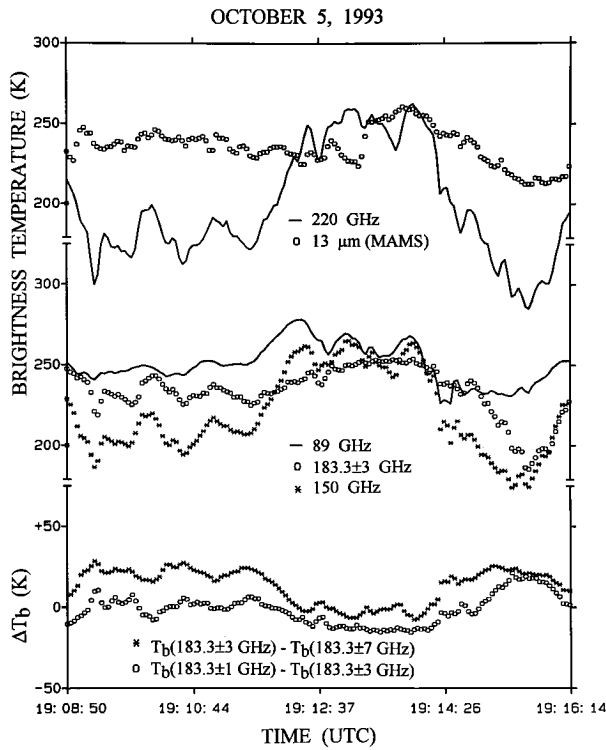


FIG. 13. Time variations of the brightness temperatures observed by MIR and MAMS aboard the ER-2 aircraft along the flight segment FL4b in Fig. 3. The brightness temperature differences from pairs of (MIR) water vapor channels are also shown in the bottom of the figure (1 min \approx 12 km).

in the convective region between 1912 and 1915 UTC, where $Z \geq 30$ dBZ. Intensive rain occurred in this region as concluded by Heymsfield et al. (1996) in their analysis of EDOP and AMPR data. The gradient of Z at height $h > 4$ km is very steep in this region, with a typical value of 5 dBZ km^{-1} . On the other hand, the gradient of Z is far more gentle above the freezing level in the stratiform region. Here a typical value of the observed gradient is 3 dBZ km^{-1} . This contrast is clearly indicated in the bottom panel; while there is a fair amount of separation between the 10- and 20-dBZ contours in the region of stratiform rain between 1909 and 1911 UTC, the two contours are generally more crowded together in the convective region.

Figure 13 shows the spatial variations of $T_b(v)$'s, observed by the MIR at the frequencies of 89, 150, 183.3 ± 3 , and 220 GHz, and by the thermal infrared channel ($\sim 13 \mu\text{m}$) of the MAMS along the same flight segment. In the bottom part of the figure, the variations of $\Delta T_b(183.3 \pm 1, 183.3 \pm 3)$ and $\Delta T_b(183.3 \pm 3, 183.3 \pm 7)$ are also displayed. Several distinct features like those in the 19 January 1993 case (Fig. 9) are again observed. These include the general correlation in the $T_b(v)$ variations between different channels of the MIR, the lack of correlation between the $T_b(v)$'s of the thermal IR and the MIR channels, and the general tracking be-

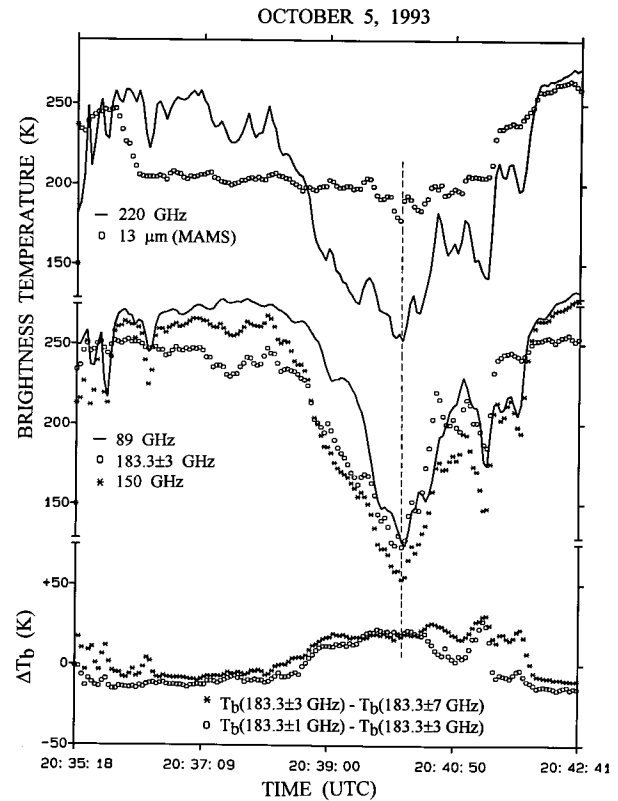


FIG. 14. Time variations of the brightness temperatures observed by MIR and MAMS aboard the ER-2 aircraft along the flight segment FL5 in Fig. 3. The brightness temperature differences from pairs of (MIR) water vapor channels are also shown in the bottom of the figure (1 min \approx 12 km).

tween the $\Delta T_b(v_1, v_2)$'s of the water vapor channels and the $T_b(v)$'s at all MIR channels. There is no evidence of a deep convective cell in this flight segment from the examination of the MIR data. The $T_b(v)$ values at $13 \mu\text{m}$ displayed in the top of the figure are greater than 210 K. This is consistent with the radar reflectivity profiles, shown in Fig. 12, of the EDOP. A comparison between either the 10- or 20-dBZ contour in Fig. 12 with $\Delta T_b(183.3 \pm 1, 183.3 \pm 3)$ or $\Delta T_b(183.3 \pm 3, 183.3 \pm 7)$ shows a certain correlation between the EDOP- and MIR-measured parameters. This suggests a potential of using the measurements from the water vapor channels to delineate the distribution of frozen hydrometeors. The data acquired from all three sensors in the flight segments FL2, FL3, and FL4a basically yield the same conclusions.

Figure 14 shows the spatial variations of $T_b(v)$'s and $\Delta T_b(v_1, v_2)$'s observed from both MIR and MAMS during the flight segment FL5. The $T_b(13 \mu\text{m})$ from the MAMS displays fairly sharp transitions at 2036 and 2041 UTC, implying the appearance and disappearance of high altitude clouds. Just like the previous case, the variations of $T_b(v)$ and $\Delta T_b(v_1, v_2)$ from MIR show very little resemblance to that of $T_b(13 \mu\text{m})$. For most of the

October 5, 1993

o FL5

* FL2, FL3, FL4a, FL4b

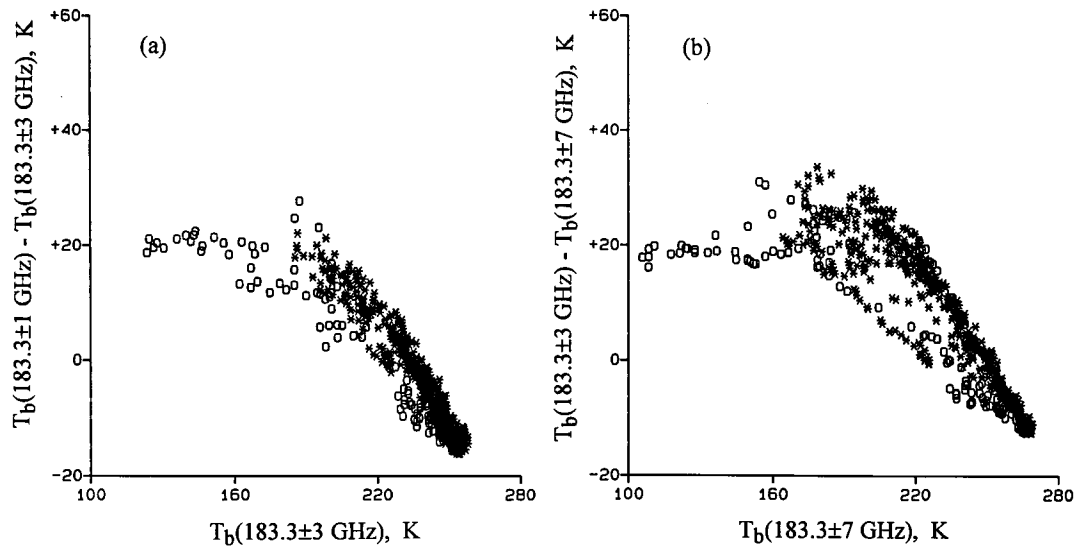


FIG. 15. The scatterplot of brightness temperature difference and brightness temperature from pairs of MIR water vapor channels.

interval between these two times, the variations of $T_b(13 \mu\text{m})$ are within ± 5 K, while excursions of the MIR $T_b(\nu)$'s exceed ± 50 K. In the neighborhood of 2040 UTC (indicated by the vertical dashed line), $T_b(13 \mu\text{m})$ values fall below 200 K, and both $T_b(150)$ and $T_b(220)$ drop to values near 100 K. This particular convective cell gives every indication of one with a strong updraft of hydrometeors like the previous one displayed in Fig. 9. The variations of $\Delta T_b(183.3 \pm 1, 183.3 \pm 3)$ and $\Delta T_b(183.3 \pm 3, 183.3 \pm 7)$ at the bottom of the figure again show a general inverse relationship with $T_b(\nu)$'s for the entire interval, with the exception of the region at and around the cell with a strong updraft.

The scatterplots of $\Delta T_b(183.3 \pm 1, 183.3 \pm 3)$ and $T_b(183.3 \pm 3)$, and of $\Delta T_b(183.3 \pm 3, 183.3 \pm 7)$ and $T_b(183.3 \pm 7)$ are displayed in Figs. 15a and 15b, respectively. The data points acquired from the first four flight segments (FL2, FL3, FL4a, and FL4b) are denoted by stars, while those from the last flight segment (FL5), by open circles. The distribution of data points from the first four flight segments in both plots (a) and (b) clearly follows the general pattern of the inverse relationship between $\Delta T_b(\nu_1, \nu_2)$ and $T_b(\nu_2)$ established previously for the 19 January 1993 case. The majority of the data points from the flight segment FL5 also follow this general pattern, but about 25–30 points show a level off or, in plot (b), even a slight decrease with a further decrease in $T_b(183.3 \pm 7)$. This leveling off or decrease is similar to features observed in plots (a) and (b) of Fig. 11 and is attributed to a convective cell with strong updraft of hydrometeors. A close examination of plots (a) and (b) in both Figs. 11 and 15 reveals a subtle difference be-

tween the two deep convective cells. While $\Delta T_b(183.3 \pm 3, 183.3 \pm 7) \approx 3\text{--}4$ K at $T_b(183.3 \pm 7) \approx 105$ K in plot (b) of Fig. 11, $\Delta T_b(183.3 \pm 3, 183.3 \pm 7) \approx 18$ K at $T_b(183.3 \pm 7) \approx 105$ K in plot (b) of Fig. 15. This suggests that more water vapor is present in the path between MIR and the deep convective cell observed on 5 October 1993 over southern Florida than that observed on 19 January 1993 over the western Pacific Ocean.

Figure 16 shows the scatterplots of the $\Delta T_b(\nu_1, \nu_2)$'s and the averages of EDOP reflectivities in four different combinations of altitude ranges and frequency channels: plots (a) and (b) are for 6–12 km, and plots (c) and (d), for 8–12 km; plots (a) and (c) are for $\Delta T_b(183.3 \pm 1, 183.3 \pm 3)$, and plots (b) and (d) for $\Delta T_b(183.3 \pm 3, 183.3 \pm 7)$. Data from all four flight segments, FL2, FL3, FL4a, and FL4b, are entered in the figure. Data from intervals of convective regions, such as that from 1911:30 to 1914:10 UTC in Fig. 12, are excluded from the plots. Generally, there is a large scatter in the data, but a positive correlation between $\Delta T_b(\nu_1, \nu_2)$ and Z is also noticed in all four plots. Similar scatter and correlation are observed when $T_b(\nu)$ values at each of the six MIR frequencies are plotted against the Z 's (not shown). The positive correlation between $\Delta T_b(\nu_1, \nu_2)$ from the water vapor channels and Z is consistent with the results of model simulation shown in Fig. 6. The large scatter in these plots is most likely caused by the large variations in the atmospheric parameters such as the particle size distribution and density in the hydrometeor profiles and the water vapor profiles from one scattering cell to another.

OCTOBER 5, 1993

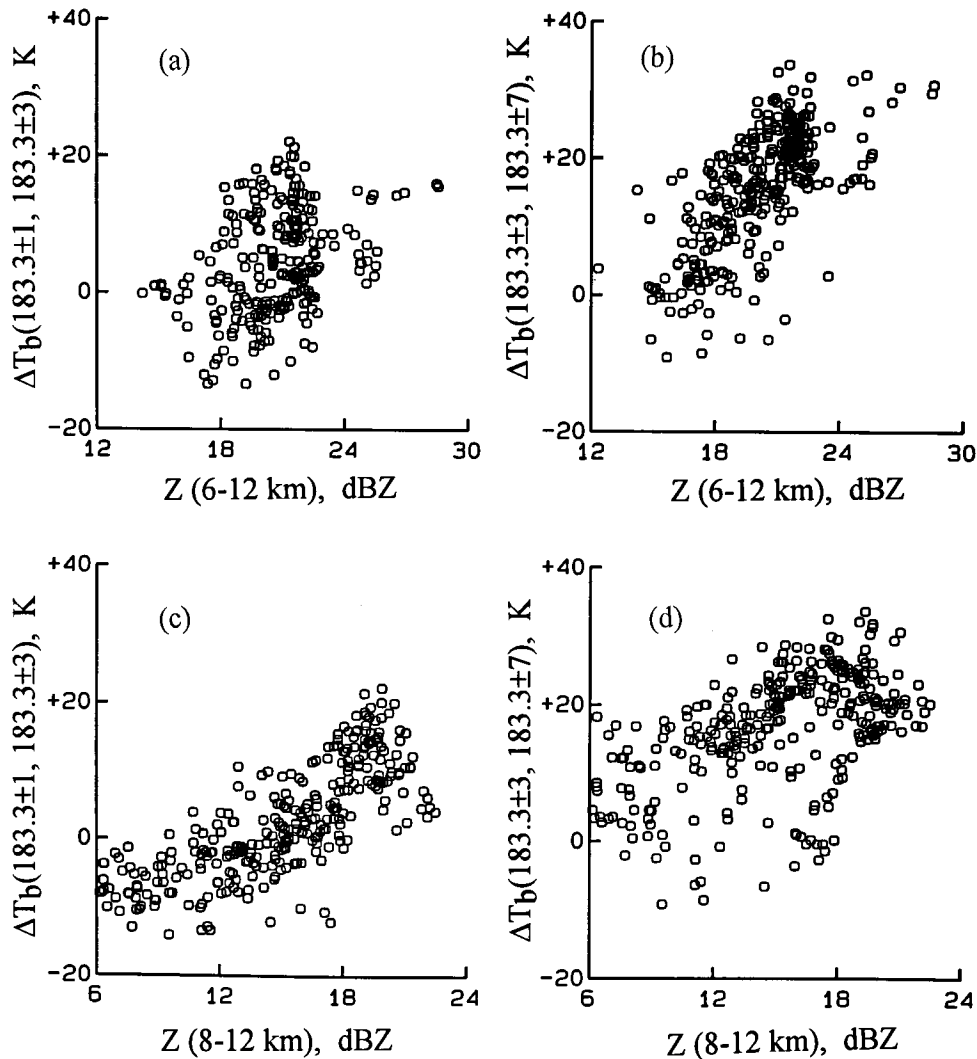


FIG. 16. The scatterplot of the brightness temperature difference in the MIR water vapor channels and average reflectivity measured by EDOP over two different altitude ranges of 6–12 and 8–12 km.

5. Discussion

The strong depression in $T_b(v)$'s experienced by all three 183.3-GHz channels over the precipitating systems discussed above suggests that the atmosphere above the scattering media is relatively dry. The radiometric signatures displayed by these channels, although far more complex, are analogous to those observed by Wang et al. (1989) for the case of a very dry atmosphere over a cold ocean background. These authors analyzed the radiometric signatures of dry atmospheres through radiative transfer calculations and compared the calculated results with the data acquired by the AMMS at 183.3 ± 2 , 183.3 ± 5 , and 183.3 ± 9 GHz to infer the amount of total precipitable water over an ocean surface following a cold-air outbreak. Similar calculations were

made at 183.3 ± 1 , 183.3 ± 3 , and 183.3 ± 7 GHz for dry atmospheres with different distributions of relative humidity profiles; the results are plotted in Fig. 17 for comparison with the observations. The top half of the figure shows the variations of $T_b(v)$'s at these frequencies with the total precipitable water W in g cm^{-2} . The bottom half of the figure gives the variations of $\Delta T_b(v_1, v_2)$ with W . Notice that at $W > 0.7 \text{ g cm}^{-2}$ the atmosphere becomes opaque to all three water vapor channels and $T_b(v)$ values monotonously decrease with increasing W ; $T_b(183.3 \pm 1)$ assumes the lowest value because its weighting function peaks at the highest altitude among the three channels. The interesting features occur in the region with $W < 0.7 \text{ g cm}^{-2}$ where $T_b(v)$'s and $\Delta T_b(v_1, v_2)$'s show more rapid changes. As W decreases, the

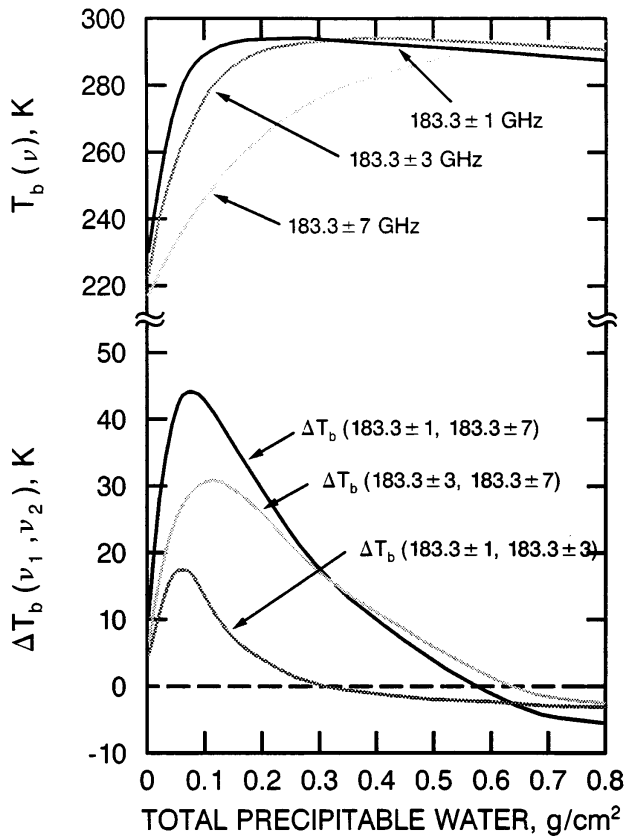


FIG. 17. The variations of brightness temperatures calculated for the three channels near 183.3 GHz and their differences against the total precipitable water for a clear and dry atmosphere over a water surface with emissivity of 0.7 and temperature of 295 K.

183.3 \pm 7-GHz channel begins to see the cold surface background, and $T_b(183.3 \pm 7)$ is the first to show a decrease. This is followed in sequence by the 183.3 \pm 3- and the 183.3 \pm 1-GHz channels as W decreases further. The 183.3 \pm 7-GHz curve intersects the 183.3 \pm 3-GHz curve at $W \cong 0.63 \text{ g cm}^{-2}$, and then the 183.3 \pm 1 curve at $W \cong 0.58 \text{ g cm}^{-2}$. The 183.3 \pm 3-GHz curve intersects the 183.3 \pm 1 curve at $W \cong 0.31 \text{ g cm}^{-2}$. This sequence of occurrences is observed by the MIR from data collected over scattering cells.

In Fig. 18a and 18b, respectively, we plot portions of the $\Delta T_b(\nu_1, \nu_2)$ data of the 183.3-GHz channels from the 19 January and 5 October cases in more detail. The time intervals are selected to include the deep convective cells. The times when the lowest $T_b(\nu)$ values in all three channels occur are indicated by the arrows. The dotted horizontal lines in the figure provide a reference where $\Delta T_b(\nu_1, \nu_2)$'s change sign. A close examination of the figure reveals that, going from the quiescent to the scattering media, the $\Delta T_b(183.3 \pm 3, 183.3 \pm 7)$ curve changes from negative to positive values first. This crossover from negative to positive regions is followed in sequence by the $\Delta T_b(183.3 \pm 1, 183.3 \pm 7)$ and $\Delta T_b(183.3 \pm 1, 183.3 \pm 3)$ curves without exception.

This sequence of crossovers is reversed when leaving from the scattering to the quiescent media. Even the observed $\Delta T_b(\nu_1, \nu_2)$'s over the small and weak scattering cell at about 0453 UTC in Fig. 18a follow this general trend. Once crossing these thresholds to the region of scattering, the atmospheric conditions correspond to the region with $W < 0.33 \text{ g cm}^{-2}$ in Fig. 17. The $\Delta T_b(\nu_1, \nu_2)$'s first increase and then decrease with the decrease in $T_b(\nu)$'s [compare Figs. 17 and 18 with plots (a) and (b) in Figs. 11 and 15]. When $\Delta T_b(\nu_1, \nu_2)$ becomes small, like the value of $\Delta T_b(183.3 \pm 3, 183.3 \pm 7)$ at the lowest $T_b(183.3 \pm 7)$ in plot (b) of Fig. 11, there is very little water vapor above the scattering media. Comparing the trends in plots (a) and (b) of Fig. 18 [or plots (a) and (b) in Figs. 11 and 15], one can safely infer that there is less water vapor above the scattering media for the deep convective cell observed on 19 January than the one on 5 October. In addition, $\Delta T_b(183.3 \pm 3, 183.3 \pm 7)$ has the lowest absolute values in the quiescent region where $\Delta T_b(\nu_1, \nu_2)$'s are negative. The $\Delta T_b(183.3 \pm 1, 183.3 \pm 7)$ curve, after a brief crossing over with the $\Delta T_b(183.3 \pm 1, 183.3 \pm 3)$ curve, assumes the highest absolute values. These observed features are consistent with those implied in Fig. 17.

It is emphasized that the curves in Fig. 17 are derived from radiative transfer calculations based on clear and dry atmospheres over ocean with emissivity of approximately 0.7 near 183 GHz. These curves are not expected to account for all the subtle features displayed in Fig. 18. For instance, in Fig. 17 the values of $\Delta T_b(183.3 \pm 1, 183.3 \pm 3)$ are generally much smaller than those of $\Delta T_b(183.3 \pm 3, 183.3 \pm 7)$ at $W < 0.5 \text{ g cm}^{-2}$, while most of the data in Fig. 18 show, in the positive region, the values of $\Delta T_b(183.3 \pm 1, 183.3 \pm 3)$ either comparable to or larger than those of $\Delta T_b(183.3 \pm 3, 183.3 \pm 7)$. At the location of the strongest $T_b(\nu)$ depression in Fig. 18a (indicated by the arrow), $\Delta T_b(183.3 \pm 3, 183.3 \pm 7) \approx 5 \text{ K}$ while $\Delta T_b(183.3 \pm 1, 183.3 \pm 3) \approx 20 \text{ K}$. The curves in the bottom of Fig. 17 show that $\Delta T_b(183.3 \pm 3, 183.3 \pm 7)$ is always greater than $\Delta T_b(183.3 \pm 1, 183.3 \pm 3)$ as long as $W < 0.5 \text{ g cm}^{-2}$. These deviations result from two very different atmospheric conditions: one with a layer of water vapor above scattering media, and the other with a dry atmosphere over oceans. They could be corrected by changing the parameters in the radiative transfer calculations. As an example, when the surface emissivity is changed from 0.7 to 0.3 and the small amount of atmospheric water vapor is limited to altitudes of 9–12 km, the calculations, with $W = 0.005 \text{ g cm}^{-2}$, give the values of 213.6, 188.8, and 183.2 K for $T_b(183.3 \pm 1)$, $T_b(183.3 \pm 3)$, and $T_b(183.3 \pm 7)$, respectively. At $W = 0.029 \text{ g cm}^{-2}$, the calculated values for $T_b(183.3 \pm 1)$, $T_b(183.3 \pm 3)$, and $T_b(183.3 \pm 7)$ are 257.5, 216.0, and 190.8 K, respectively. These calculated results give larger $\Delta T_b(183.3 \pm 1, 183.3 \pm 3)$ than $\Delta T_b(183.3 \pm 3, 183.3 \pm 7)$. In fact, at $W = 0.005 \text{ g cm}^{-2}$, $\Delta T_b(183.3 \pm 1, 183.3 \pm 3) = 24.8 \text{ K}$ and $\Delta T_b(183.3 \pm 3, 183.3$

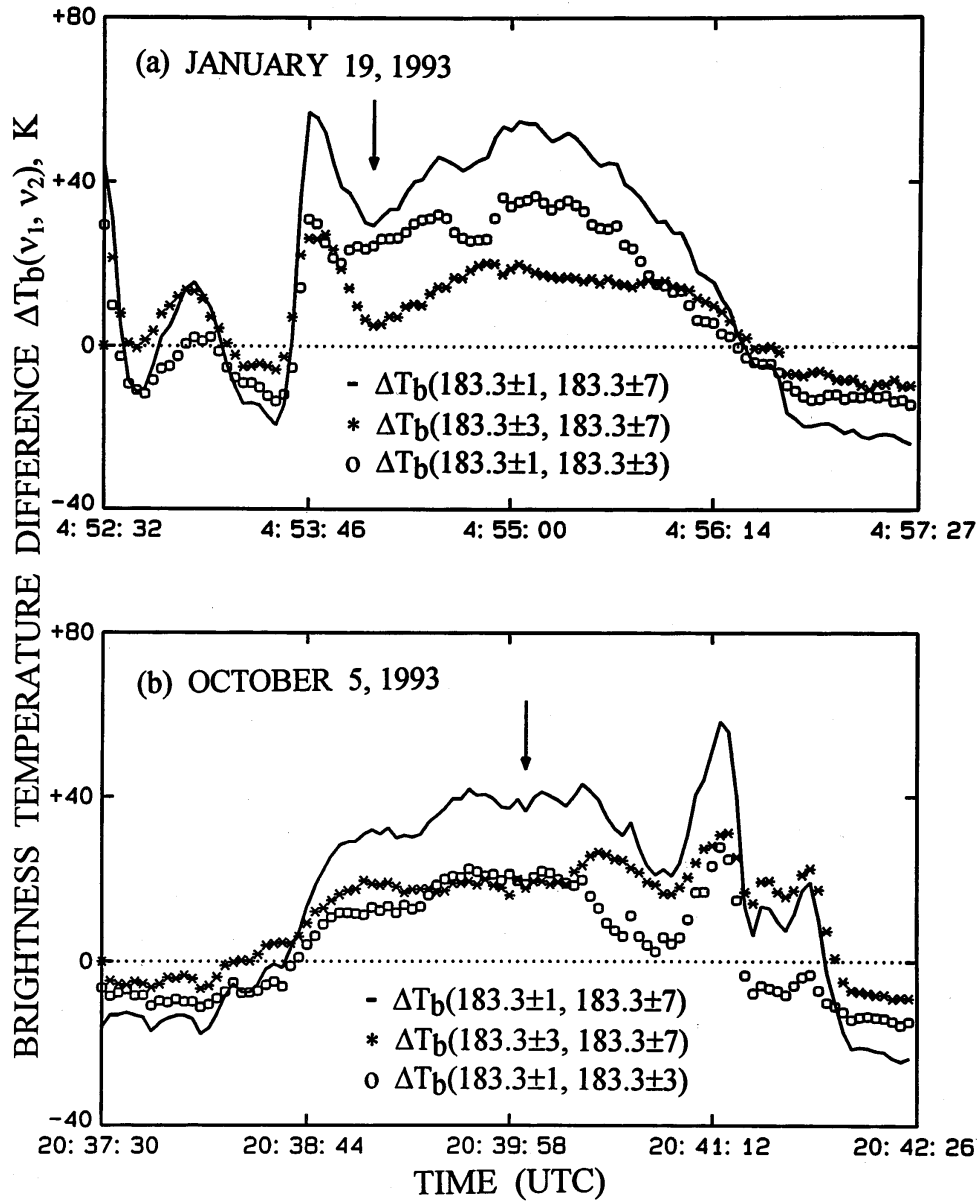


FIG. 18. The time variations of the brightness temperature differences observed from the MIR water vapor channels on (a) 19 January 1993 and (b) 5 October 1993.

$\pm 7) = 5.6$ K, which are comparable to those observed at the location of lowest $T_b(v)$ depression in Fig. 18a.

The calculations above imply that the values of $T_b(v)$ strongly depend on the background emissivity as well as the altitude of the water vapor layer. For that matter, the values of W in Fig. 17 cannot be taken seriously to infer the amount of the water vapor above the scattering media. To achieve a good agreement between the measurements and calculations requires a sophisticated cloud model that provides microphysical description of hydrometeor profiles for a variety of storm cells, including the towering ones reported in this paper. The

radiative transfer calculations, including scattering, will have to be made based on these hydrometeor profiles. One may even have to vary further the amount of water vapor at and above the scattering media in order to fully understand the radiometric signatures from these water vapor channels. The task of analyzing these signatures is complicated and challenging. However, it is quite possible that the radiometric signatures from these water vapor and other channels could provide the means of estimating the amount of water vapor as well as mapping the distribution of frozen hydrometeors of the storm cells.

6. Conclusions

Radiometric measurements from an MIR aboard the NASA ER-2 aircraft were made from an altitude of 20 km at the frequencies of 89, 150, 183.3 ± 1 , 183.3 ± 3 , 183.3 ± 7 , and 220 GHz over two different storms; one was located in the Pacific Ocean near 1°S , 156°E on 19 January 1993 and another in southern Florida on 5 October 1993. These measurements are complemented by observations from other sensors aboard the same aircraft or in the NASA DC-8 aircraft flying along the same path at a lower altitude of 11 km. In the first case on 19 January a host of microwave radiometers covering a frequency range of 18–183 GHz were aboard the DC-8 aircraft, and the MODIS Airborne Simulator was aboard the same ER-2 aircraft. In the second case on 5 October only the ER-2 aircraft carrying a 9.7-GHz Doppler radar (EDOP) and MAMS was involved. The analysis of the MIR data from the measurements of three water vapor channels near 183.3 GHz was emphasized because these channels were found to contain very useful information and were least explored in the previous studies on rain storms. Radiative transfer and radar reflectivity calculations based on the hydrometeor profiles generated by the RAMS cloud model (Smith et al. 1992) were made to help interpret the observed data. It was found from both observations and calculations that, over the storm cells, the differences in brightness temperatures from pairs of water vapor channels correlated with the brightness temperatures themselves. Because of the double side-band measurements of these channels, this correlation was proven to be caused by water vapor in and over the scattering media.

From the thermal infrared channel of MAS or MAMS and the sounding data, the cloud top over the storm area was estimated to be at an altitude of about 13–14 km for both measurement cases. The brightness temperatures of the thermal infrared channel did not show much variation, while those from all the MIR channels were found to vary significantly. This suggests the potential of using these channels to map regions of frozen hydrometeors associated with storms. The differences in brightness temperatures from pairs of the water vapor channels showed a definite correlation with the average radar reflectivity in the 6–12-km altitude range, similar to the correlation between brightness temperatures at millimeter wavelengths and radar reflectivity reported from previous studies (Wang et al. 1994; Heymsfield et al. 1996). For both cases of observations, the ER-2 aircraft flew over a deep convective cell that was characterized by MAMS (MAS) thermal infrared temperatures of less than 190 K. These cells were also characterized by small differences in the MIR water vapor channels at very low brightness temperatures.

There is an analogy between the radiometric signatures of the water vapor channels observed over the storm-associated scattering media and those over a dry atmosphere with a cold ocean background. The ob-

served behavior of the brightness temperature differences from these channels, when entering the scattering cells, corresponds well to that entering the region of dry atmosphere. The changes of these brightness temperature differences follow the same particular sequence as the total precipitable water decreases over the ocean background or above the scattering media. Even for the two deep convective cells, it is possible to compare the measured brightness temperature differences and relatively infer the amount of water vapor above the scattering media. However, a quantitative estimation of water vapor above the scattering media cannot be obtained from the analogy of radiometric signatures from these two very different atmospheric conditions. Systematic calculations based on a variety of model-generated hydrometeor and water vapor profiles, as well as more observations, are needed to learn more about the radiometric signatures from these and other millimeter-wave channels.

Acknowledgments. The authors thank Dr. W. Olson for critical comments on this paper and Dr. G. Heymsfield for supplying the EDOP data. This study is supported by Dr. R. K. Kakar, manager of NASA's Mesoscale Atmospheric Dynamics Program.

REFERENCES

- Adler, R. F., R. A. Mack, N. Prasad, H.-Y. M. Yeh, and I. M. Hakkarinen, 1990: Aircraft microwave observations and simulations of deep convection from 18 to 183 GHz. Part I: Observations. *J. Atmos. Oceanic Technol.*, **7**, 377–391.
- , A. J. Negri, P. R. Keehn, and I. M. Hakkarinen, 1993: Estimation of monthly rainfall over Japan and surrounding waters from a combination of low-orbit microwave and geosynchronous IR data. *J. Appl. Meteor.*, **32**, 335–356.
- Bauer, P., and N. C. Grody, 1995: The potential of combining SSM/I and SSM/T2 measurements to improve the identification of snowcover and precipitation. *IEEE Trans. Geosci. Remote Sens.*, **33**, 252–261.
- Chang, A. T. C., A. Barnes, M. Glass, R. Kakar, and T. T. Wilhelm, 1993: Aircraft observations of the vertical structure of stratiform precipitation relevant to microwave radiative transfer. *J. Appl. Meteor.*, **32**, 1083–1091.
- Cotton, W. R., G. J. Tripoli, R. M. Rauber, and E. A. Mulvihill, 1986: Numerical simulation of the effects of varying ice crystal nucleation rates and aggregation processes on orographic snowfall. *J. Climate Appl. Meteor.*, **25**, 1658–1680.
- Hakkarinen, I. M., and R. F. Adler, 1988: Observations of convective precipitation at 92 and 183 GHz: Aircraft results. *Meteor. Atmos. Phys.*, **38**, 164–182.
- Heymsfield, G. M., I. J. Caylor, I. M. Shepherd, and W. B. Olson, 1996: Structure of Florida thunderstorms using high-altitude aircraft radiometer and radar observations. *J. Appl. Meteor.*, **35**, 1736–1762.
- Kakar, R. K., 1983: Retrieval of clear sky moisture profiles using the 183 GHz water vapor line. *J. Climate Appl. Meteor.*, **22**, 1282–1289.
- Kummerow, C., 1993: On the accuracy of the Eddington approximation for radiative transfer in the microwave frequencies. *J. Geophys. Res.*, **98**, 2757–2765.
- , and L. Giglio, 1994: A passive microwave technique for estimating rainfall and vertical structure information from space. Part I: Algorithm description. *J. Appl. Meteor.*, **33**, 3–18.

- , R. A. Mack, and I. M. Hakkarinen, 1989: A self-consistency approach to improve microwave rainfall estimates from space. *J. Appl. Meteor.*, **28**, 869–884.
- Lutz, R., T. T. Wilheit, J. R. Wang, and R. K. Kakar, 1991: Retrieval of atmospheric water vapor profiles using radiometric measurements at 183 and 90 GHz. *IEEE Trans. Geosci. Remote Sens.*, **29**, 602–609.
- McClatchey, R. A., R. W. Fenn, J. E. A. Selby, F. E. Volz, and J. S. Garing, 1972: Optical properties of the atmosphere (third edition). Environmental Research Papers No. 411. Air Force Cambridge Research Laboratory, Bedford, MA, 108 pp.
- Negri, A. J., R. F. Adler, E. J. Nelkin, and G. J. Huffman, 1994: Regional rainfall climatologies derived from Special Sensor Microwave/Imager (SSM/I) data. *Bull. Amer. Meteor. Soc.*, **75**, 1165–1182.
- Olson, W. S., C. D. Kummerow, G. M. Heymsfield, I. J. Caylor, and L. Giglio, 1996: A method for combined passive-active microwave retrievals of cloud and precipitation profiles. *J. Appl. Meteor.*, **35**, 1763–1789.
- Prabhakara, C., D. A. Short, W. Wiscombe, R. S. Fraser, and B. E. Vollmer, 1986: Rainfall over oceans inferred from Nimbus-7 SMMR. *J. Climate Appl. Meteor.*, **25**, 1464–1474.
- Prasad, N., H.-Y. M. Yeh, R. F. Adler, and W. K. Tao, 1995: Microwave and infrared simulations of an intensive convective system and comparison with aircraft observations. *J. Appl. Meteor.*, **34**, 153–174.
- Racette, P., R. F. Adler, A. J. Gasiewski, D. M. Jackson, J. R. Wang, and D. S. Zacharias, 1996: An airborne millimeter-wave imaging radiometer for cloud, precipitation, and atmospheric water vapor studies. *J. Atmos. Oceanic Technol.*, **13**, 610–619.
- Rodgers, E. B., H. Siddalingaiah, A. T. C. Chang, and T. T. Wilheit, 1979: A statistical technique for determining rainfall over land employing Nimbus-6 ESMR measurements. *J. Appl. Meteor.*, **18**, 987–991.
- Schaerer, G., and T. T. Wilheit, 1979: A passive microwave technique for profiling of atmospheric water vapor. *Radio Sci.*, **14**, 371–375.
- Simpson, J. A., R. F. Adler, and G. North, 1988: A proposed tropical rainfall measuring mission (TRMM) satellite. *Bull. Amer. Meteor. Soc.*, **69**, 278–295.
- Smith, E. A., and A. Mugnai, 1988: Radiative transfer to space through a precipitating cloud at multiple microwave frequencies. Part II: Results and analysis. *J. Appl. Meteor.*, **27**, 1074–1091.
- , —, H. J. Cooper, G. J. Tripoli, and X. Xiang, 1992: Foundations for statistical-physical precipitation retrieval from passive microwave satellite measurements. Part I: Brightness-temperature properties of a time-dependent cloud-radiation model. *J. Appl. Meteor.*, **31**, 506–531.
- Spencer, R. W., 1986: A satellite passive 37 GHz scattering based method for measuring oceanic rain rates. *J. Climate Appl. Meteor.*, **25**, 754–766.
- , H. M. Goodman, and R. E. Hood, 1989: Precipitation retrieval over land and ocean with the SSM/I. Part I: Identification and characteristics of the scattering signal. *J. Atmos. Oceanic Technol.*, **6**, 254–273.
- , R. E. Hood, F. J. LaFontaine, E. A. Smith, R. Platt, J. Gagliano, V. L. Griffin, and E. Lobl, 1994: High-resolution imaging of rain systems with the Advanced Microwave Precipitation Radiometer. *J. Atmos. Oceanic Technol.*, **11**, 849–857.
- Tripoli, G. J., 1992: A nonhydrostatic model designed to simulate scale interaction. *Mon. Wea. Rev.*, **120**, 1342–1359.
- Vivekanandan, J., J. Turk, and V. N. Bringi, 1993: Comparisons of precipitation measurements by the Advanced Microwave Precipitation Radiometer and multiparameter radar. *IEEE Trans. Geosci. Remote Sens.*, **31**, 860–870.
- Wang, J. R., and Coauthors, 1983: Profiling atmospheric water vapor by microwave radiometry. *J. Climate Appl. Meteor.*, **22**, 779–788.
- , T. T. Wilheit, and L. A. Chang, 1989: Retrieval of total precipitable water using radiometric measurements near 92 and 183 GHz frequencies. *J. Appl. Meteor.*, **28**, 146–154.
- , R. Meneghini, H. Kumagai, T. T. Wilheit, W. C. Bonczyk, P. Racette, J. R. Tesmer, and B. Maves, 1994: Airborne active and passive microwave observations of super typhoon Flo. *IEEE Trans. Geosci. Remote Sens.*, **32**, 231–242.
- , S. H. Melfi, P. Racette, D. N. Whiteman, L. A. Chang, R. A. Ferrare, K. D. Evans, and F. J. Schmidlin, 1995: Simultaneous measurements of atmospheric water vapor with MIR, Raman lidar, and rawinsondes. *J. Appl. Meteor.*, **34**, 1595–1607.
- Weinman, J. A., and P. J. Guetter, 1977: Determination of rainfall distribution from microwave radiation measured by the Nimbus-6 ESMR. *J. Appl. Meteor.*, **16**, 437–442.
- , R. Meneghini, and K. Nakamura, 1990: Retrieval of precipitation profiles from airborne radar and radiometer measurements: Comparison with dual-frequency radar measurements. *J. Appl. Meteor.*, **29**, 981–993.
- Wilheit, T. T., A. T. C. Chang, M. S. V. Rao, E. B. Rodgers, and J. S. Theon, 1977: A satellite technique for quantitatively mapping rainfall rates over the oceans. *J. Appl. Meteor.*, **16**, 551–560.
- , and Coauthors, 1982: Microwave radiometric observations near 19.35, 92, and 183 GHz of precipitation in tropical storm Cora. *J. Appl. Meteor.*, **21**, 1137–1145.
- , —, and L. S. Chiu, 1991: Retrieval of monthly rainfall indices from microwave radiometric measurements using probability distribution function. *J. Atmos. Oceanic Technol.*, **8**, 118–136.
- Wu, R., and J. A. Weinman, 1984: Microwave radiances from precipitating clouds containing aspherical ice, combined phase and liquid hydrometeors. *J. Geophys. Res.*, **89**, 7170–7178.
- Yeh, H.-Y. M., N. Prasad, R. A. Mack, and R. F. Adler, 1990: Aircraft microwave observations and simulations of deep convection from 18–183 GHz. Part II: Model results. *J. Atmos. Oceanic Technol.*, **7**, 392–410.